

Laser Medicine and Medical Imaging

Sponsors

National Institutes of Health
U.S. Air Force – Office of Scientific Research
U.S. Navy – Office of Naval Research/MFEL
Whittaker Foundation

Project Staff

Stephen A. Boppart, Ravi K. Ghanta, Pei-Lin Hsiung, Tony Ko, Constantinos Pitris, Kathleen Saunders, Dr. Mark E. Brezinski, Dr. Christian Chudoba, Dr. Wolfgang Drexler, Dr. Ingmar Hartl, Dr. Xingde Li, Dr. Uwe Morgner, Dr. Joel Schuman, Dr. Debra L. Stamper, Professor James G. Fujimoto

1. OCT Technology

High resolution and Novel Sources for OCT Imaging

Optical coherence tomography (OCT) is an emerging technology for micron-scale cross-sectional imaging of biological tissue [1, 2]. Enhancing the resolution of OCT images continues to be a very active field of research. The longitudinal resolution in OCT images is inversely proportional to the optical bandwidth and proportional to the square of the center wavelength of the light source. Ultrahigh resolution OCT requires extremely broad bandwidths because of this $\lambda^2/\Delta\lambda$ dependence of the longitudinal resolution. This is particularly the case for the spectral region between 1.2 μm and 1.5 μm . This spectral region is of high interest for OCT because of the high penetration depth in biological tissue and the possibility of performing spectral resolved imaging of water absorption bands. Superluminescent diodes are used in conventional OCT systems and typically yield 10-15 μm longitudinal resolutions. We demonstrated previously OCT imaging with resolutions of 1 μm at 800 nm [3] and 5.1 μm at 1300 nm [4] in biological tissue using a Kerr-lens mode-locked Ti:sapphire laser with double-chirped mirrors and the self phase modulation broadened spectrum of a Kerr-lens mode-locked Cr:forsterite laser, respectively.

These broadband Kerr-lens mode-locked lasers are not available commercially and require expensive and hard to fabricate double chirped mirrors. We tested a novel broad band light source that uses continuum generation in an air-silica microstructured fiber for the application in OCT. High nonlinearity, air-silica microstructure fibers [5] or tapered fibers [6] can generate an extremely broadband continuum using low energy femtosecond pulses. These fibers achieve high nonlinearities by using a tight mode confinement and shifting the zero of dispersion to shorter wavelengths.

We successfully demonstrated the use of continuum generation in an air-silica microstructure fiber for OCT imaging [7]. We achieved a free-space longitudinal resolution of 2.5 μm at a 1.3 μm center wavelength and demonstrated the application of the OCT system for *in vivo* imaging of biological tissue. These are the highest resolutions achieved to date for imaging in this wavelength regime.

Figure 1 (left) shows a schematic of the experimental setup. We launched 100 fs pulses generated by a commercial Kerr-lens modelocked Ti:Sapphire laser, which was pumped by a frequency doubled Nd:Vanadate laser into a 1 m length of microstructure fiber. The fiber continuum was collimated with a microscope objective (MO), spectrally filtered by a long-pass filter and focussed with a chromatically corrected custom-designed lens (AL) into a dispersion shifted single mode fiber. A custom-designed lens and broadband 3dB fiber couplers (FC), designed for 1300 nm center wavelength (FC), were used in the OCT setup. Since the light source had excess amplitude noise, a dual balanced detection with two InGAs photodiodes (D1,

D2) was used. Polarization controllers (PC) minimized the polarization mismatch of the interferometer arms to avoid degradation of the shape and the peak height of the interference fringes.

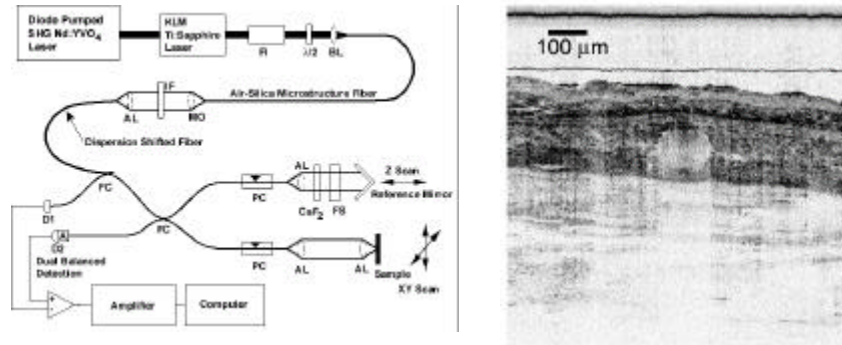


Figure 1: Left: Ultrahigh resolution OCT system using continuum generation in an air-silica microstructure fiber as the light source. See text for explanation of the acronyms. Right: *In vivo* ultrahigh resolution ($\sim 6 \times 2.5 \mu\text{m}$, transverse \times longitudinal resolution, $1.0 \times 1.0 \text{ mm}$; 1000×3000 pixels) OCT image of a Syrian hamster cheek pouch. Different layers are clearly visible.

We demonstrated the feasibility of *in vivo* ultra high resolution imaging by using the cheek pouch of a Syrian hamster, a well-established animal model for studies of cancer progression. Fig. 1 (right) shows an *in vivo* image of cheek pouch which shows the epithelium, connective tissue and muscle layers at ultrahigh resolution. The cheek pouch was index matched by using a microscope cover glass and saline solution.

Spectroscopic OCT

Relatively few studies on spectroscopic OCT have been performed because broadband light sources have not been available. An earlier study of spectroscopic OCT used a bandwidth of $\sim 50 \text{ nm}$ at $1.3 \mu\text{m}$ [8]. We recently used a Kerr-lens modelocked Ti:Sapphire laser with dispersion compensation by double chirped mirrors for spectroscopic imaging in the wavelength range from 650 to 1000 nm [9]. Previous spectroscopic OCT studies in the spectral region of the water absorption band at $1.45 \mu\text{m}$ used two different light sources in dual wavelength OCT systems. One light source was used for absorption measurements and the second light source for referencing [10, 11]. However, this approach adds the noise of two independent light sources, and accurate referencing is hard to achieve.

In order to demonstrate spectroscopic OCT imaging of differential water absorption we selected a spectral range of 200 nm centered at 1400 nm from the continuum. We imaged a phantom consisting of two microscope cover glasses of $170 \mu\text{m}$ thickness confining a water sample. A schematic of the setup is shown in Fig. 2 (left). The cover glasses were in contact at one side of the sample and had a spacing of $\sim 0.8 \text{ mm}$ at a lateral distance of 10 mm . The focal position of the imaging beam was $\sim 0.4 \text{ mm}$ above the bottom coverglass.

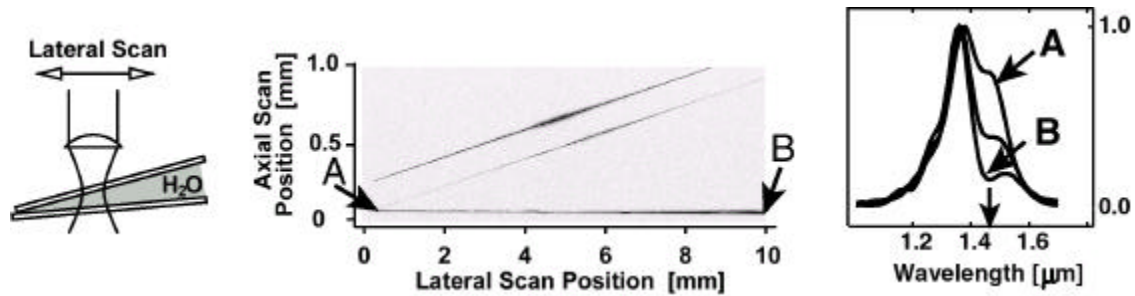


Figure 2: Left: The phantom consists of two microscopy cover glasses enclosing H₂O as absorber. Center: Digitally demodulated OCT image of the phantom used for this study. Right: Spectrum of the OCT echo of the cover glass surface at the points indicated with A and B and one intermediate point. The arrow indicates wavelength of the water absorption band.

The full interference signal was digitally recorded at 12 bit resolution with 30,000 digitalization points per 1.3 mm A-scan. A digitally demodulated image of the sample is shown in Fig. 2 (center). The spectrum of several A-scans was calculated by Fourier-transforming a 2000 point window centered at the maximum of the reflection signal. The spectra obtained were normalized to the intensity maximum. The spectra at the points A and B and one intermediate point are shown in Fig. 2 (right). One clearly observes that the absorption of the spectral intensity around 1.45 μm increases with increasing absorber thickness.

OCT Devices

The development of OCT imaging devices is important for clinical applications. OCT has the advantage that it is fiber optically based and can readily be integrated with a wide range of existing clinical imaging instruments including microscopes, laparoscopes, endoscopes, and catheters. Several imaging devices have been designed and developed and evaluated in both animal and preliminary clinical studies.

The success of optical coherence tomography in clinical applications will depend in large part on the design and availability of delivery mechanisms that allow seamless integration with existing diagnostic imaging modalities. As an imaging technique capable of imaging human tissue at high resolution, OCT could lead to detection of pathology at earlier stages than currently possible, leading to improved patient prognosis. Several imaging devices have been designed and developed to investigate the feasibility of OCT for the clinical assessment of pathology of a variety of non-transparent tissue *in vivo*.

OCT Colposcope

We have developed an OCT integrated colposcope that permits a simultaneous real time *en face* view of cervical pathology and OCT imaging. The system is based on a standard Zeiss colposcope. A custom attachment was designed and constructed to connect to the accessory port of the colposcope, permitting integration of OCT optics into a standard colposcopic examination. Two orthogonal scanning galvanometers are calibrated to allow scanning at an arbitrary position and orientation in a 4×4 cm area. A diagram of the system is shown in Figure 3.

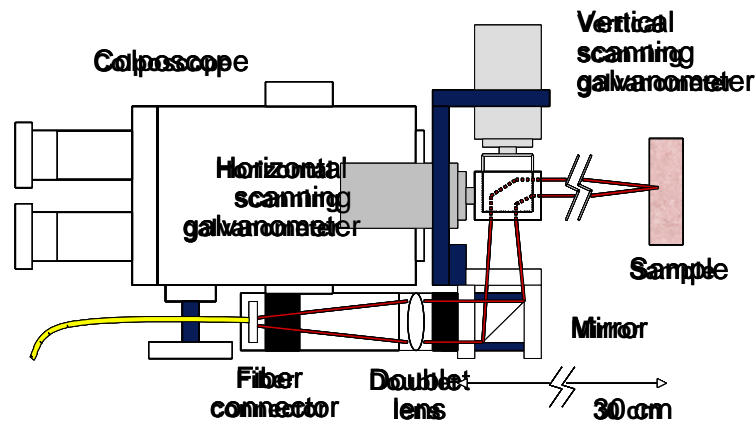


Figure 3: Diagram of the OCT integrated colposcope. The system permits simultaneous OCT and video imaging of the cervix. A large aperture doublet lens enables imaging with a transverse resolution of $30\ \mu\text{m}$ at the long 30 cm working distance of the colposcope.

The precision and noise of the driving waveforms are kept well below the resolution of the system to minimize the effect of jitter even at the large working distance of the colposcope. A visible 532 nm aiming beam at $250\ \mu\text{W}$ was used to allow the operator to direct the OCT scan in the high magnification and intense white light illuminated field of the colposcope. The focal spot size of the system is $\sim 30\ \mu\text{m}$ and the axial resolution is $\sim 15\ \mu\text{m}$. The OCT colposcope has been used in the clinical setting to successfully enable the acquisition of cross-sectional tomographic images of cervical tissue. OCT has demonstrated the ability to clearly delineate the epithelial and subepithelial structure of both normal and abnormal cervical tissue. These studies were performed in collaboration with Dr. Annkathryn Goodman from the Massachusetts General Hospital.

Doppler OCT Imaging Catheter

We have developed a miniature fiber optically based Doppler catheter that integrates functional imaging with structural imaging for OCT. The Doppler catheter can be used for assessment of blood flow within a vessel as well as the fine structures within the vessel wall. A prototype Doppler catheter with an outer diameter of $\sim 410\ \mu\text{m}$ has been developed and demonstrated for measuring the intraluminal flow profile in phantom. The Doppler OCT catheter can be potentially used for evaluating the severity of stenosis and the outcome of cardiovascular interventions such as stenting. Figure 4 shows the schematic diagram of one representative design. A single mode optical fiber is first angle cleaved at 8° to reduce back reflection and a gradient index (GRIN) lens is glued to the angle cleaved end of the fiber to focus the beam. In order to have non-zero projection of the interrogating beam along the longitudinal axis of the catheter to detect flow, an $\sim 50^\circ$ microprism is custom-made and employed to deflect the beam so the beam exits the catheter at $\sim 50^\circ$ with respect to the catheter axis. The single mode fiber, the GRIN lens and the microprism are attached to form a single unit and housed concentrically in a 27 Gauge ($\sim 410\ \mu\text{m}$) hypodermic metal guard. The entire catheter is housed within a transparent plastic sheath with a sealed distal end. At the proximal end of the catheter the hollow wire is connected to a DC motor. The optical beam can be scanned radially by rotating the hollow metal wire along with the single mode fiber and the distal optics. A rotary coupler based upon a glass capillary tube is used to connect the rotating fiber at the proximal end of the catheter and a stationary fiber from the light source [12].

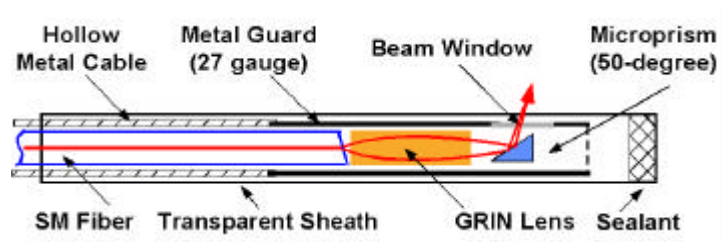


Figure 4: Schematic of a representative Doppler OCT imaging catheter design. A GRIN lens and a micoprism are used to focus and deflect the beam. The beam coming out of the catheter at $\sim 50^\circ$ with respect to the catheter longitudinal axis. A thin-wall stainless steel hypodermic tube is used to house the optical fiber and the distal end optics.

A flow phantom experiment has been conducted to validate the Doppler OCT catheter for intraluminal assessment of the cross sectional flow velocity. The fluid is 1% Intralipid corresponding to a Mie-scattering coefficient (u_s) of $\sim 86 \text{ cm}^{-1}$. The fluid is circulated through a 3.1 mm inner diameter plastic tubing and the flow rate is controlled by a precision digital pump. The catheter is introduced into the tubing through a Y-connector. The Doppler OCT signal (interference fringes) over 360° is acquired by rotating the catheter at a constant speed. The flow velocity at each pixel along the axial scan is deduced from the Doppler frequency shift with respect to the center frequency caused by a scanning reference mirror. Figure 5(b) shows representative velocity profiles at two pump flow rates. Notice that the flow velocities are zero at the surfaces of outer wall of the catheter sheath and the inner wall of the tubing, which is consistent with a laminar flow profile. The entire flow velocity profile over 360° is shown in Figure 5(b).

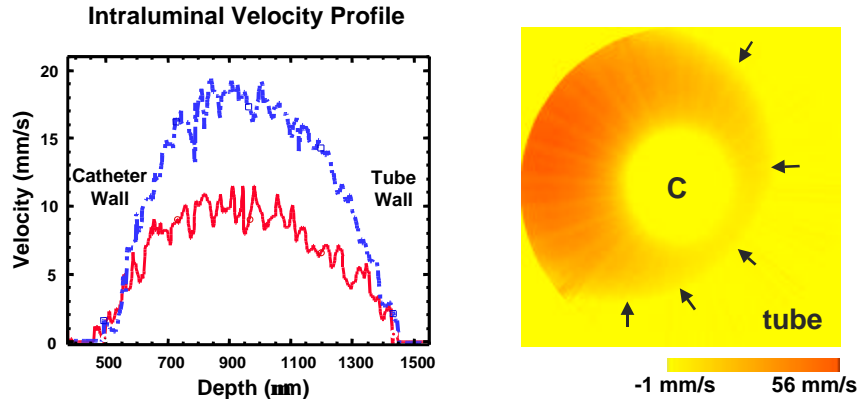


Figure 5: a) Two representative flow velocity profiles for one particular axial scans at two different pump flow rates. b) Reconstructed flow velocity profile over 360° at one pump flow rate.

For a certain portion of the radial scan, although the inner wall surface of the tubing is not reached by the OCT probing beam, the position of the wall can be deduced by extrapolating the flow velocity profile to zero. We are currently evaluating the potential of this device for deducing the vessel wall diameter in a physiologically relevant environment (blood). This device can also be used for imaging the fine structures within the vessel wall when moderate saline flushing is used. In addition to the flow velocity profile, the flow turbulence may also be quantifiable by investigating the flow velocity variance. Future work will also focus on investigating the potential of this device for diagnosis of thrombosis or aneurysm from the velocity variance assessment.

OCT Imaging Needle

OCT applications have been limited to the surfaces or lumina of organ systems because the penetration depth of OCT is ~2-3 mm in most tissues. It has not been possible in the past to image structures inside solid tissues or organs. There are, however, many clinical scenarios where high resolution imaging of solid tissues is desirable. One promising application of OCT is in imaging pathology and guiding biopsy in solid tissues. This procedure could reduce the sampling error of excisional biopsy in diagnosing cancers in solid organs such as the prostate or breast. Other applications include optical imaging in scenarios where excisional biopsy is hazardous, and in surgical guidance such as in cryosurgery or interstitial photodynamic therapy.

We have developed a prototype of an interstitial imaging needle for OCT that has a diameter as small as 27 Gauge (~410 μ m) [12]. The OCT imaging needle is inserted directly into soft solid tissues or organs to deliver, scan, and collect a single mode optical beam. Imaging can be performed up to 2-3 mm away from the needle, enabling imaging of a cylindrical volume 4-6 mm diameter by several mm in length. The small size of the OCT imaging needle permits its use in virtually any solid tissue or organ with low resistance and minimal trauma during imaging in direct contact with tissue. The small size also allows the needle to be integrated with standard biopsy devices to provide a “first look” to guide biopsies. Figure 6 shows a schematic of a representative needle design and photograph of a prototype imaging needle. A single mode optical fiber is first angle cleaved at 8° to reduce back reflection and a gradient index (GRIN) lens with a 250 μ m diameter is glued to the angle cleaved end of the fiber to focus the beam. A 90° microprism is employed to deflect the beam perpendicular to the needle axis. The single mode fiber, the GRIN lens and the microprism are attached to form a single unit with UV curing optical cement and housed concentrically in a 27 Gauge hypodermic tube. An optical window is ground on the tube and the distal end of the tube is sharpened for easy insertion.

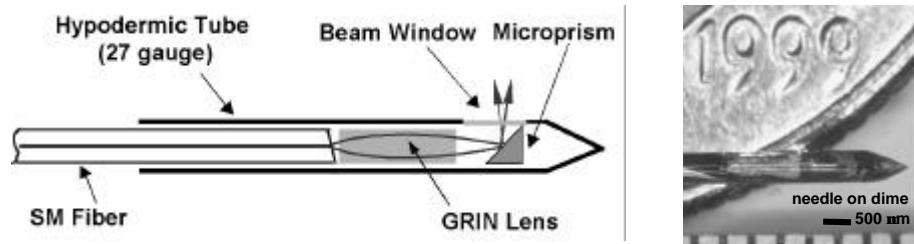


Figure 6: a) Schematic of a representative needle design. A GRIN lens and a microprism are used to focus and deflect the beam. A thin-wall stainless steel hypodermic tube is used to house the optical fiber and the distal end optics. b) Photograph of prototype OCT imaging needle on a dime.

The prototype imaging needle had a confocal parameter of ~380 μ m, corresponding to a spot size (or transverse resolution) of ~17 μ m, with a focal distance ~80 μ m outside the optical window. The optical beam can be scanned radially by rotating the entire needle along with the distal optics. This technique is similar to that used with acupuncture needles. The OCT imaging plane is perpendicular to the needle axis and the position of the imaging plane can be controlled by varying the depth of needle insertion.

High resolution imaging with the OCT needle has been demonstrated *in vivo* in an animal model. In order to achieve high resolution as well as high image penetration depths, a Kerr-lens mode-locked (KLM) Cr:Forsterite laser was used as the low coherence light source. The self-phase modulated spectral bandwidth of the laser was ~120 nm at a central wavelength of 1270 nm. The resultant axial resolution was measured to be 6.7 μ m. Imaging was performed in the leg muscle of an anesthetized hamster as an example of a solid tissue.

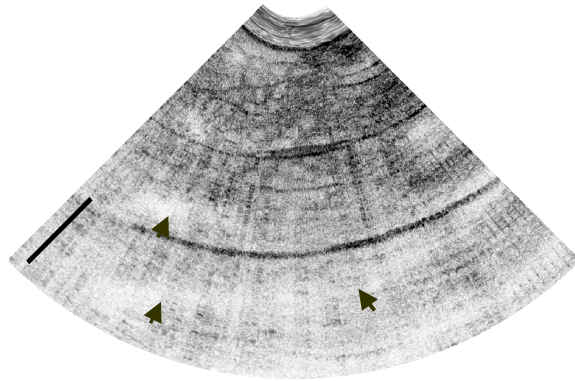


Figure 7: *In vivo* OCT image of hamster leg muscle acquired with the needle. The needle has focusing optics at the distal end. The scale bar represents 500 μm . Muscle fascicles are clearly discerned. Layered appearance resulting from muscle birefringence is also observed (indicated with arrows).

A sector OCT image was generated by scanning the needle over an angle of $\sim 90^\circ$. As shown in Figure 7, the fascicles of the muscle are clearly differentiated on the OCT image. The layered contours of maximum back-reflection indicated by arrows are the result of tissue birefringence. This preliminary data demonstrates the feasibility of using the OCT imaging needle for minimally invasive imaging of the internal structural morphology of solid tissues or organ systems.

Surgical Imaging Probe

We have designed and developed a handheld probe and demonstrated its application for imaging cartilage during open field surgery. The compact hand held probe (~ 1.5 cm in diameter and ~ 12 cm in length) consists of a Hopkins lens relay and a galvanometer mirror which steers the beam in the transverse direction with the scanning range and spot size magnified by telescope optics. The distal end of the probe is sterilizable for use in a surgical field. A similar hand held probe has been used for OCT imaging of the oral mucosa. The transverse resolution and scan range are determined by the choice of lenses in the relay system. A short working distance of ~ 0.5 - 1.5 cm is chosen to permit relatively high magnification. If necessary, a compact color or black-and-white CCD camera can be integrated into the optical system of the hand held probe to enable *en face* viewing of the tissue and OCT imaging plane. Alternately, a small coherent fiber bundle fiberscope can be used in conjunction with the hand held probe to allow direct visualization of the region being OCT imaged. The transverse resolution will be ~ 5 - 20 μm depending upon the magnification. This probe has been used with a portable OCT system at the National Cancer Institute to image oral leukoplakia and monitor pharmacological chemoprevention therapy. Recently we have designed a version of the probe that uses two orthogonally positioned galvanometer mirrors to enable scanning of the OCT beam in the *en face* plane. This will permit us to use the probe for *in vivo* investigations of optical coherence microscopy, a technique that combines standard OCT imaging with confocal microscopy.

2. Optical Biopsy using Optical Coherence Tomography

Ophthalmic Studies

OCT has perhaps been most widely investigated in ophthalmology, where it is beginning to make a clinical impact in the assessment of retinal diseases such as macular holes, age-related macular degeneration, glaucoma, and diabetic retinopathy [1, 13-15]. Current clinical practice calls for the development of techniques to diagnose ophthalmic disease in its early stages, when treatment is most effective and significant irreversible damage can either be prevented or delayed. With typical axial resolutions of 10 μm , OCT already provides more detailed structural information than any other conventional imaging technique. However, the detection of many of the early changes associated with diseases can require more accurate quantification of retinal structure than is possible with standard resolution OCT.

Using the broad bandwidth of our ultrahigh resolution OCT system, we can image with axial resolutions greater than 3 μm (in the retina), corresponding to a factor of 5 improvement over OCT technology using superluminescent diode sources. The signal to noise ratio for the system is ~ 100 dB. This system enables a significant improvement in the visualization of intraretinal structures for earlier diagnosis and more precise staging of pathology (Figure 8). To our knowledge, the image shown in Figure 1 represents the highest resolution *in vivo* image ever acquired of the human retina. Ultrahigh resolution OCT offers an unprecedented visualization of retinal morphology with structures such as the retinal nerve fiber layer, retinal pigment epithelium, and the inner and outer plexiform layers. These structures are relevant in a variety of retinal diseases, including age-related macular degeneration, diabetic retinopathy, and glaucoma (the three leading causes of blindness worldwide).

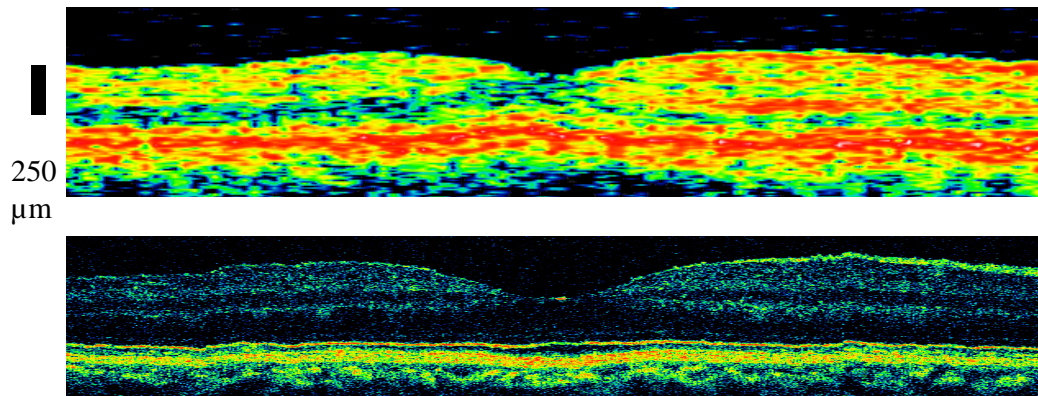


Figure 8: *In vivo* standard resolution (top) and ultrahigh resolution (bottom) OCT images of a normal human fovea at approximately the same site. Resolutions were 10-15 μm (axial) x 15 μm (transverse) and 3 μm (axial) x 15 μm (transverse) respectively.

Image processing techniques can be applied to acquired tomograms to quantify retinal and intraretinal structures relevant to disease. Figure 9 illustrates the application of preliminary image processing segmentation algorithms to ultrahigh resolution OCT images to quantify retinal and intraretinal structures. Ultrahigh resolution enables the quantification of layers relevant to retinal disease, which were previously not visualized or quantified using standard resolution OCT. Precise quantification of the retinal thickness is important for the diagnosis and staging of macular edema and diabetic retinopathy. Quantification of the photoreceptor and Henle's layer may be important in a variety of retinal diseases. Quantification of the ganglion cell layer and the nerve fiber layer is important in retinal diseases such as glaucoma.

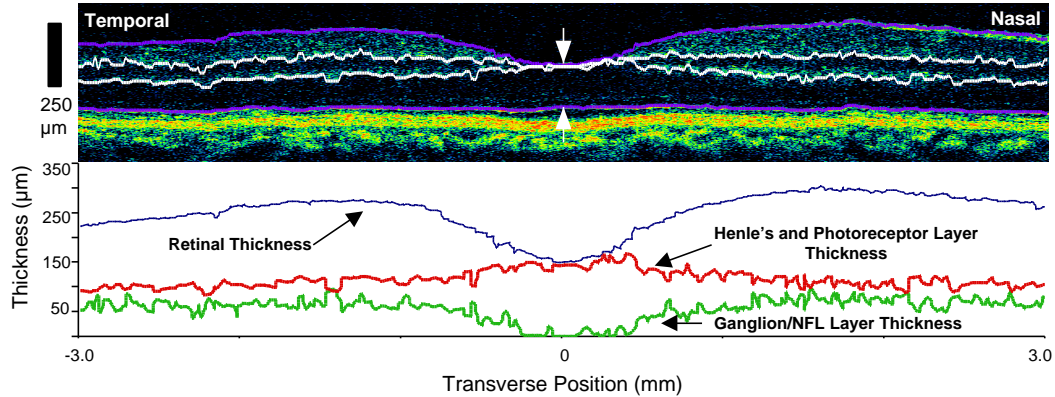


Figure 9: Ultrahigh resolution allows for an unprecedented visualization of intraretinal structures which may be quantified to provide an objective measure of retinal disease.

The visualization and quantification of retinal and intraretinal layers should serve as a valuable clinical tool for the early assessment of ophthalmic disease. This concept has already been demonstrated in a mouse retinal disease model. Using the ultrahigh resolution OCT system, we have imaged and identified the many intraretinal layers of the mouse retina. Figure 10 illustrates the ability for ultrahigh resolution OCT to visualize the intraretinal layers of a normal mouse retina *in vivo*. The different intraretinal layers can be clearly identified in the OCT image: Nerve Fiber Layer (NFL), Inner Plexiform Layer (IPL), Inner Nuclear Layer (INL), Outer Plexiform Layer (OPL), Outer Nuclear Layer (ONL), Retinal Pigment Epithelium (RPE). When compared with histology taken from the same animal, the ultrahigh resolution OCT image corresponds well with the layers identified in the histology.

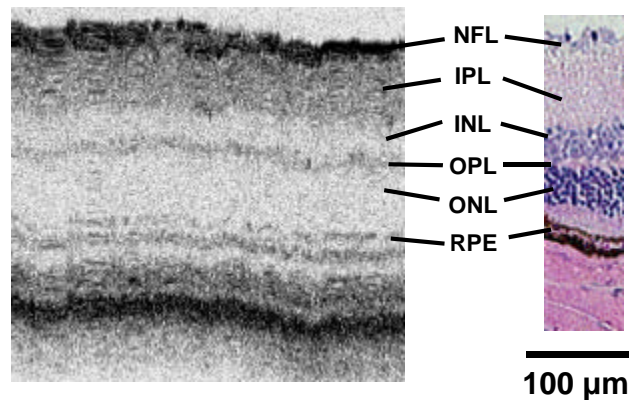


Figure 10: *In vivo* ultrahigh resolution OCT image of a normal mouse retina and corresponding histology. The layers identified in the OCT images correspond well with the layers identified in the histology.

In the rhodopsin knockout mouse, the outer plexiform and outer nuclear layers undergo degeneration three months postpartum. Figure 11 illustrates the differences between the *in vivo*

OCT images of a normal mouse retina and a rhodopsin knockout mouse retina. At 5 months of age, the outer plexiform layer and the outer nuclear layer of the rhodopsin knockout mouse retina would have undergone degeneration. When comparing the knockout mouse retina with the normal wild type mouse retina, the OCT image clearly demonstrates this degeneration in the knockout mouse. The *in vivo* ultrahigh resolution OCT images clearly depict the degeneration of the outer plexiform and the outer nuclear layer in the rhodopsin knockout mouse retina.

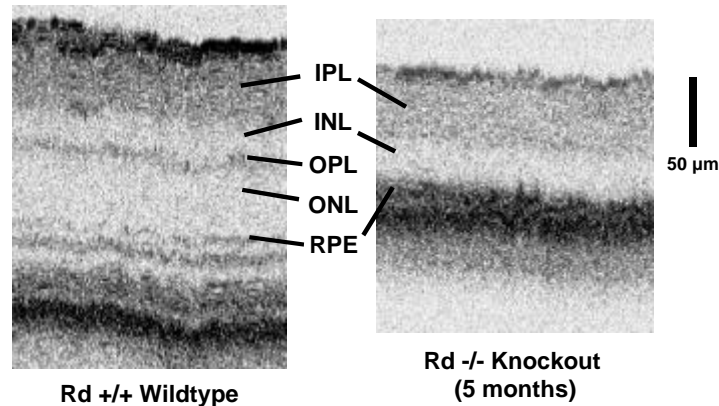


Figure 11: *In vivo* ultrahigh resolution OCT image of a normal mouse retina (Rd +/+ wild type) and a rhodopsin knockout mouse retina (Rd -/-). OCT has the ability to quantify the thickness of the different intraretinal layers as well as track disease progression in a non-invasive manner.

This demonstrates that ultrahigh resolution OCT can be used to identify different intraretinal layers, quantify layer thickness, and track retinal disease progression. Future work will involve ultrahigh resolution OCT imaging studies of patients with retinal diseases such as age-related macular degeneration, diabetic retinopathy, and glaucoma.

Arterial Imaging *In Vivo*

Guided placement of intracoronary stents has greatly improved the outcome of interventional intravascular procedures and constitutes the majority of current percutaneous interventions [16, 17]. Simultaneous intravascular imaging has advanced our knowledge about stenting and may improve immediate and long-term results [18, 19]. In the CRUISE study, a 44% reduction was seen in the need for revascularization after IVUS guidance [19]. However, IVUS has several limitations. At 40 MHz, IVUS has a resolution of only ~80 µm, which does not allow adequate interpretation of some arterial structures such as the fibrous cap of a plaque. Second, the ultrasound transducer is mounted on a separate catheter, requiring the balloon catheters to be removed before the ultrasound catheter can be introduced. While attempts have been made to develop a commercially available ultrasound guidewire, they have not been successful. IVUS catheters are also expensive, making them impractical for routine clinical use.

OCT has several advantages for intravascular imaging. First, the resolution of OCT is between 4-15 µm, depending on the light source used. Second, OCT is fiber-optically based, allowing extremely small catheters to be produced. Recently, an OCT imaging probe was developed with an outer diameter of ~400 µm [12]. The small size and lack of a transducer make the probability high that an OCT guidewire could be developed. Third, OCT catheters consist of relatively simple optical components, making them relatively inexpensive. Fourth, OCT systems are compact and portable, about the size of an ultrasound machine or smaller. Finally, OCT imaging is performed near real time, with current catheter-based systems operating at 4-8 frames per second [20]. We have explored the feasibility of catheter-based *in vivo* OCT imaging performed in conjunction with stent deployment in New Zealand White Rabbit aortas. OCT imaging is compared with high

frequency IVUS for its ability to assess stent apposition to the vessel wall. An *in vitro* stent model was also used for quantitative evaluation of OCT in assessing stent apposition.

Figure 12(a) illustrates a representative OCT image of a stented rabbit abdominal aorta. Structures such as the media (and a small portion of adventitia) can be clearly identified. Stent struts are sharply differentiated from the aorta wall. Due to the highly scattering nature of stent struts, shadows throughout the media and adventitia are produced on the OCT image. IVUS image of the registered site was also taken with a 30 MHz catheter shown in Figure 12(b).

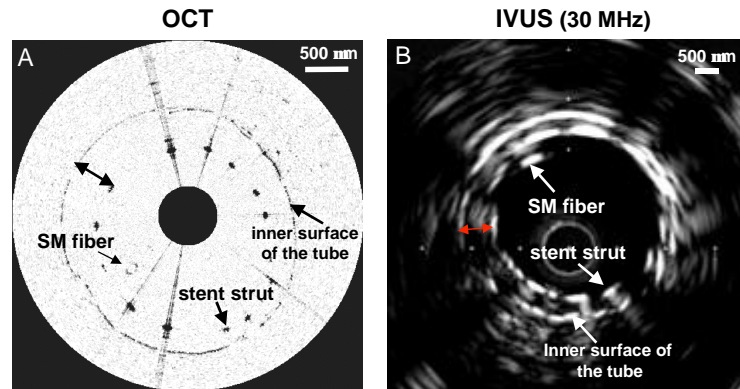


Figure 12: OCT and 30 MHz IVUS images of a stent model that was submerged in saline are respectively shown in A and B. The stent struts, a single mode optical fiber within the stent and the inner surface of the flexible plastics tube are clearly defined on the OCT image. Compared with IVUS, the superior OCT resolution permits more accurate determination of the maximum and minimum separation between the stent and the inner surface of the tube.

In comparison, the IVUS image lacks clarity in discerning the stent struts from the vessel wall and the media. Compared with the IVUS image, the superior resolution of OCT makes it considerably easier to differentiate the stent from the arterial wall on the OCT image. This work strongly suggests that OCT with its superior resolution and image contrast could have a huge potential impact on the guidance of intravascular interventional procedures. These studies were performed in collaboration with Dr. Herman Gold from the Massachusetts General Hospital and Dr. Neil Weissman from Washington Hospital Center.

Hamster Cheek Pouch *In Vivo* Tissue Preservation Study

To date, many previous studies have compared *ex vivo* OCT imaging to histopathology. While some tissues, such as arterial pathology or cartilage, are relatively stable post mortem, others, such as epithelial tissues, exhibit rapid degradation. It is therefore important to preserve these tissues with minimal changes in morphology. The goal of this study is to investigate the difference between *in vivo* and *ex vivo* OCT imaging and the effect of different preservation solutions on image quality using the hamster cheek pouch. The hamster cheek pouch was chosen because of its easy access and because it is a well established model for carcinogenesis and cancer progression. The advent of the ultrahigh resolution OCT imaging technology is important for this study because it enables changes in tissue morphology that may have been difficult to resolve with standard resolution OCT imaging to be clearly visualized.

OCT imaging was performed using an ultrahigh resolution OCT imaging system [3]. An axial resolution of 2 μm and a transverse resolution of 5 μm were employed. Several different preservation solutions were evaluated including: saline at low temperature, saline at room temperature, phosphate buffered sucrose (PBS140), University of Wisconsin solution (UW), and

10% formalin. Phosphate buffered sucrose and University of Wisconsin solution are common tissue preservation solutions, while formalin is commonly used for tissue fixation before histological processing. Following the anesthetization of the animal, the imaging areas in the cheek pouch were marked with india ink. For each imaging site, a 0.75 mm (axial) by 1 mm (transverse) OCT image was obtained. Each image consisted of 2000 axial pixels and 1000 transverse pixels to ensure that the pixel density was sufficient for high resolution imaging. The multiple imaging sites were then resected and the specimens placed in room temperature saline, chilled saline, PBS140, UW or 10% formalin. The marked areas in the different preservation solutions were imaged at 30, 50, and 70 minutes post mortem. The image quality, details, and contrast for each solution were then compared. At the conclusion of the experiments, the tissue was fixed in formalin and histologically processed.

Figure 13 shows an example of OCT imaging data, which is a compilation of the *in vivo* images, the effects of different preservation solutions at 70 minutes postmortem, and the corresponding histology. The top row (a-e) represents *in vivo* OCT images of the hamster cheek pouch tissue taken at different imaging sites. The middle row (f-j) represents *ex vivo* OCT images of the same imaging site as the top row taken at 70 minutes postmortem. These areas were imaged *ex vivo* while preserved in a saline ice bath (f), room temperature saline (g), phosphate buffered sucrose 140 (h), University of Wisconsin solution (i) and 10% formalin (j). All the OCT images were collected at a resolution of $2\ \mu\text{m} \times 5\ \mu\text{m}$ at 800 nm central wavelength. The bottom row represents the corresponding histology stained with Trichrome. The histology slides are viewed at 40x and were scaled to match the image size.

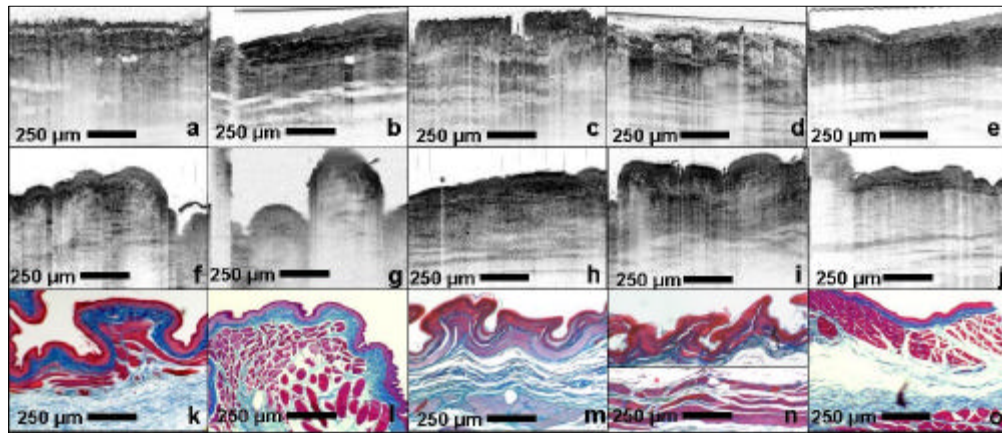


Figure 13: In vivo (a-e) and 70 min. postmortem ex vivo (f-j) ultrahigh resolution OCT images of the hamster cheek pouch tissue under different preservation solutions and their corresponding histologic cross-sections stained with Trichrome (k-o).

Evaluation of these images indicates that most changes in optical properties and OCT contrast in tissue occur within minutes after excision for all preservation solutions but formalin. The contrast between the epithelial cells and the stratum corneum as well as the underlying connective tissue is rapidly lost in almost all solutions, with the exception of formalin. The low backscattering nature of the dense connective tissue is not preserved. This could be the result of leakage of intracellular material from the cells into the extracellular space or expansion of the spaces between the normally dense collagen fibers. In formalin, the reflection of the two layers above and below the epithelial cells increases in intensity. Modification of the backscattering intensity of the lower, looser collagen fibers is also visible *ex vivo*. The epithelial layer, which is often the region of interest in neoplastic imaging, appears to be very sensitive to *ex vivo* preservation conditions. Although formalin is used routinely for histological processing, it has long been considered a poor option for tissue preservation in optical imaging studies because it changes the fluorescent and optical properties of tissue. However, our study indicates that formalin may

actually be a better preservative for *ex vivo*, morphological OCT imaging. If the goal of the study is to image and evaluate variations in tissue morphology, then fixation may change the contrast of some compartments, but it also appears to better maintain the architectural features of interest.

Clinical Orthopedics Imaging

Osteoarthritis (OA) is the leading cause of chronic disability in developed countries, symptomatically affecting about 14% of the adult population in the United States alone [21]. The earliest pathological changes are collagen disorganization, an increase in the water content, and alteration in glycosaminoglycans (GAGS) [22]. Among the later changes are cartilage loss (thinning effect), fibrillation, and surface erosion [22]. Until recently, osteoarthritis has been accepted as an inescapable consequence of aging. There is now strong evidence that osteoarthritic progression can be slowed or modified through surgical and/or pharmacological intervention [23, 24]. However, current imaging technologies have only a limited ability to monitor changes in articular cartilage. This deficiency is the basis of the current NIH OA initiative to find solutions to this major healthcare dilemma [25]. Currently available techniques such as plain film and magnetic resonance imaging (MRI) have resolutions of no better than 10 mm, which limits their use in monitoring cartilage changes [21, 26-28]. Although arthroscopy is widely used in diagnosis of joint disorders [29], it provides magnified views of only the articular surface. Thus, the pathologic changes under the articular cartilage surface cannot be visualized. A diagnostic imaging technique capable of high-resolution imaging of articular cartilage *in vivo* would be invaluable to detect disease, to follow its progression and to monitor therapeutic effectiveness.

OCT could potentially overcome the limitations of the current orthopedic and rheumatologic imaging modalities for office-based imaging. Real time OCT imaging was performed *in vivo* during open knee surgery to demonstrate the feasibility of OCT for assessing normal and osteoarthritic joint cartilage morphology. OCT imaging permitted a complete survey of the exposed joint cartilage morphology within a few minutes. In addition to structural morphology, polarization sensitivity was also assessed with real time OCT. Figure 14 illustrates a representative OCT image and the corresponding histology of Grade 2 osteoarthritic knee cartilage. The slight irregularities of the cartilage surface can be clearly seen in both the OCT image and corresponding histology section. In the OCT image the layered pattern was also observed; however the pattern was interrupted and can only be found on the upper portion of the cartilage below the surface. This loss of the layered image pattern suggests a loss of collagen structural organization. Abnormal changes can also be seen in the histology as a loss of pericellular staining and hypercellularity (arrows).

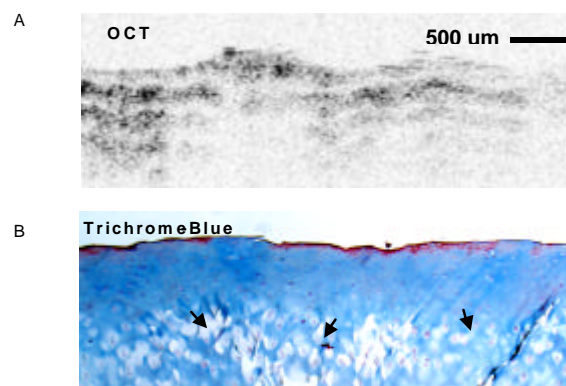


Figure 14: (a) OCT image of articular cartilage demonstrating some birefringence in the superficial zones with loss of birefringence in the deeper zones signifying early degeneration. (b) Histology of the same section reveals superficial zone of relatively normal cartilage with deeper zones of cartilage displaying depletion of peri-cellular staining (arrows).

The current study demonstrated osteoarthritic changes in cartilage could be assessed at a resolution higher than any current clinical technology. In addition, polarization sensitivity was demonstrated *in vivo*, and in this small sample of patients, the loss of polarization correlated with the degree of disease. Future investigations will work to improve the technology, develop new methods to quantify polarization data as well as examine absorption spectroscopy. Future work will also focus on developing a small OCT catheter that can be used for intra-articular imaging of the joint cartilage in conjunction with arthroscopy. As stated previously, changes in water content are an early sign of osteoarthritis. Since water strongly absorbs at approximately 1500 nm, by imaging at both 1300 nm and 1500 nm, it is theoretically possible to measure water content of cartilage. These studies were conducted in collaboration with Dr. Scott Martin at Brigham and Women's Hospital.

3. Early Neoplastic Diagnosis

Prostate

Prostate carcinoma is the second leading cause of death among men in the United States [30, 31]. The clinical outcome of prostate carcinoma is closely related to histologic differentiation and malignancy grade. Although well-differentiated tumors do not significantly affect patient survival, a poor degree of tumor differentiation has a major impact on prognosis [32, 33]. Current biopsy techniques often incur high rates of sampling errors and inaccurate patient diagnosis [34]. A risk assessment tool that can accurately grade carcinoma progression and tissue dysplasia in the prostate could have significant clinical impact in early diagnosis and treatment [35].

Preliminary studies have been conducted using optical coherence tomography (OCT) as an imaging modality to assess tissue microstructures *in vivo* and in real time on human prostatic tissue [36]. OCT can be used as an "optical biopsy" to provide ultrahigh resolution images of tissue morphology *in vivo*. Figure 15 shows an example *ex vivo* OCT image of human prostate tissue. Glandular lumens as well as lipid filled structures in the fibroadipose tissue can be distinguished are correlated between the OCT image (top) and tissue photomicrograph (bottom).

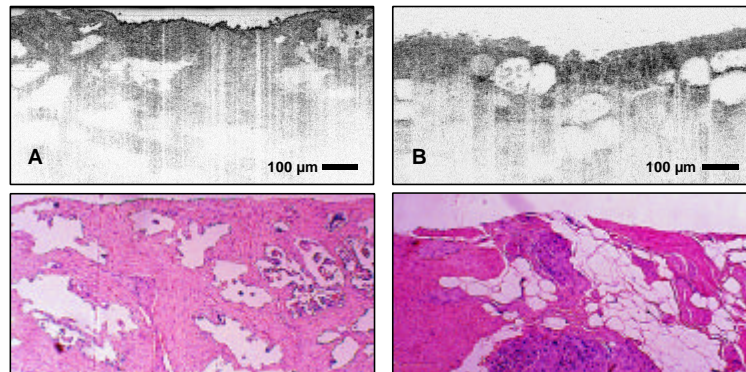


Figure 15: OCT images (top) and photomicrographs (bottom) of human prostate *ex vivo* showing a) benign glandular lumens and b) lipid filled structures in fibroadipose tissue.

With the ability to diagnosis cellular level ($<10\ \mu\text{m}$) features, OCT has the potential to grade dysplasia at different stages of prostate tumor progression without the need to excise tissue samples for conventional biopsy histological analysis. Future work will develop and apply microstructural imaging using minimally invasive imaging devices for guiding biopsy and reducing sampling errors. These studies establish the basis for future clinical studies in both animals and patients. In the past, typical image resolution in clinical systems was $10\ \mu\text{m}$ – $15\ \mu\text{m}$. Using broadband $\text{Ti:Al}_2\text{O}_3$ laser sources, cellular level features have been delineated with $1\text{-}2\ \mu\text{m}$

resolution [3]. The development of new laser sources operating at higher wavelengths (1300 nm) will allow greater image penetration depths of 2-3 mm which could increase the efficacy of OCT in neoplastic tissue diagnosis. If successful, this technology could improve the diagnosis and management of prostate cancer by reducing false negatives in biopsy and permit a more comprehensive determination of the locus of cancer. In a more general context, the technology and protocols developed would enable the ultrahigh resolution imaging of architectural morphology and differentiation of pathology in solid organs and create a new paradigm for image guided excisional biopsy which could have widespread clinical and research applications.

Female Reproductive System

The dysplastic human cervix is an excellent model system that can be used to systematically investigate and quantitatively evaluate OCT *in vivo*. Although the incidence of cervical neoplasia is very common, there are only 13,700 new cervical cancer cases per year resulting in 4,900 deaths in the United States [37]. Early identification of cervical neoplasia improves patients' prognosis; the screening technique of choice, the Papanikolaou Smear, despite its accuracy shortcomings, has significantly contributed to the reduction of deaths associated with cervical cancer. Neoplasias are most responsive to medical intervention at early stages, prior to undergoing metastasis. When these disorders arise from known premalignant states, and if a detection method exists, high risk populations can be screened to reduce patient morbidity and mortality.

The diagnosis of neoplasia and early cancer is based on colposcopy and biopsy, i.e. the visual examination of the surface of the cervix under high magnification and white light illumination and the simultaneous acquisition of biopsies. Dysplastic changes of the cervical epithelial layer have been extensively examined and the progression of dysplasia to cancer has been carefully mapped both histologically and colposcopically [38, 39]. Changes associated with neoplasia include cellular and microstructural alterations. The well defined pathology, progression, and endpoints, along with ease of accessibility and frequency of colposcopic procedures, make the cervix a good model system for the evaluation of the diagnostic capabilities of OCT. It is unlikely that OCT imaging will have a direct clinical application for cervical cancer detection. However, OCT imaging studies in the cervix can provide insight into the relationship of OCT images to the architectural and cellular morphology of tissues as well as the mechanisms of contrast in OCT images and tissue optical properties. Conclusions can be drawn which are generalizable to other epithelial cancers.

We have performed ongoing OCT imaging studies of cervical cancer with a prototype OCT colposcope. This design enables *en face* viewing of pathology on the surface of the cervix, while simultaneously controlling the scan pattern of the OCT image. We have imaged 24 patients to date. Figure 16 shows an example OCT image of a normal cervix, a colposcopic view of the area scanned, and corresponding histology. Differences were observed between normal and abnormal tissue with various pathologies and between different grades of dysplasia. The epithelium, sub-epithelial glands, endocervical canal, and vaginal fornix were clearly visible.

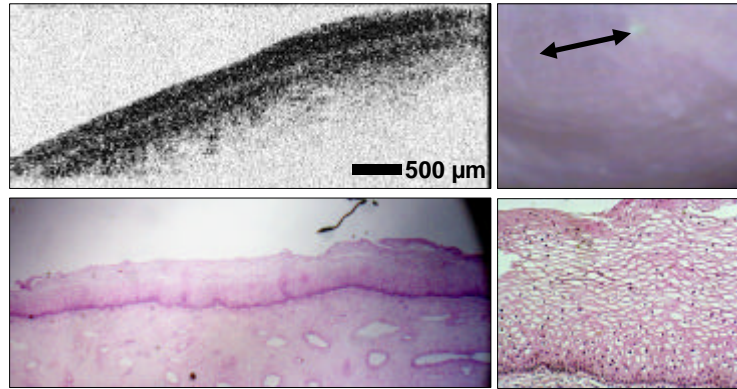


Figure 16: OCT image of a normal cervix, a colposcopic view of the area scanned, and corresponding histology.

Figure 17 shows an example of OCT images of a normal and severe squamous dysplasia from the same patient. In dysplasia, the epithelial layers were irregular with no clear borders. Higher backscattering intensity was also observed in areas with dysplasia or cancer. Further work is needed to determine whether OCT can accurately differentiate between high grade and low grade dysplasia.

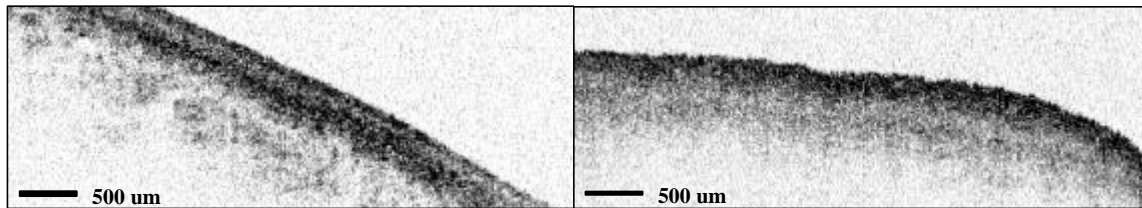


Figure 17: Preliminary OCT images of normal (left) and severe squamous dysplasia (right) from the same patient. In dysplasia, the epithelial layers were irregular with no clear borders. Higher backscattering intensity was also observed in areas with dysplasia or cancer.

This data is preliminary and we are currently corroborating our findings with pathologists. These studies are being performed in collaboration with Dr. Annekathryn Goodman from the Massachusetts General Hospital.

Gastrointestinal Tract

Barrett's esophagus is believed to be caused by chronic gastroesophageal reflux [40]. Several studies have demonstrated that Barrett's esophagus is associated with a 30-125 times increased risk of developing adenocarcinoma. For this reason, endoscopic surveillance of Barrett's epithelium every 12-18 months is recommended [41]. Endoscopic screening currently involves random four-quadrant biopsies every 1-2 cm along the length of suspect mucosa. However, random biopsies are prone to sampling errors and small foci of carcinoma or dysplasia may be missed [42, 43]. Because of the imprecision and high cost associated with screening, new methods are being developed to assess patients at increased risk. Endoscopic ultrasound catheters have been used clinically for imaging the Barrett's metaplasia with 50-100 μm resolution [44]. However, these resolutions are insufficient to resolve early epithelial changes

which occur in Barrett's esophagus and the pre-malignant changes which lead to adenocarcinoma of the esophagus.

We have performed endoscopic OCT imaging of the human esophagus in patients with Barrett's esophagus. Endoscopic OCT was performed using both linear and radial scanning methods to evaluate scanning techniques and to demonstrate the ability to discern changes in architectural morphology associated with Barrett's esophagus [12]. Continuous OCT imaging was performed at 4 frames per second using either linear- or radial-scanning OCT catheter/probes. Figures 18A-18C show a representative linear scan OCT image, an endoscopic video image, and biopsy histology of normal squamous epithelium. The OCT image (4 mm x 2.5 mm, 512 x 256 pixels) of normal epithelium in Figure 18C illustrates the relatively homogeneous epithelium (ep), the high-backscattering region (appearing darker) of the lamina propria (lp), the low-backscattering muscularis mucosa (mm), the high-backscattering submucosa (sm), and the low-backscattering and thick muscularis propria (mp). The epithelial layer in the OCT image was relatively homogeneous correlating with the histology of a fragment of squamous epithelium. The biopsy specimen was interpreted as normal squamous mucosa. Images were also acquired from regions of Barrett's epithelium in the same patient. Figures 18D-18F show an OCT image (4 mm x 2.5 mm, 512 x 256 pixels) of an abnormal esophageal region, an endoscopic video image, and the biopsy histology. The video image reveals a finger-like projection of abnormal epithelium that appears pink.

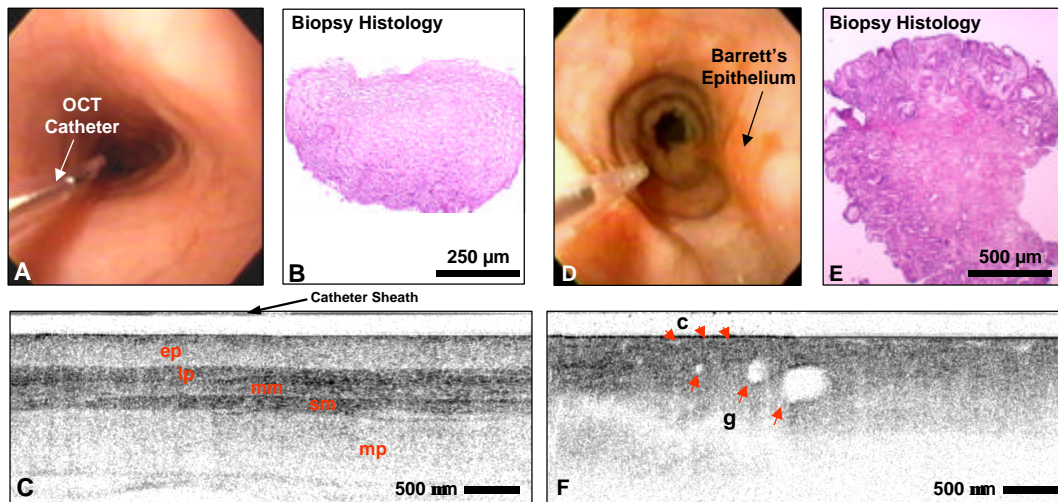


Figure 18: Clinical endoscopic OCT imaging of normal and Barrett's esophagus using linear scanning. (a) Endoscopic video image of normal region. (b) Biopsy histology of normal squamous epithelium. (c) OCT image of normal squamous epithelium with relatively uniform and distinct layered structures. (d) Endoscopic video image of region showing finger-like projection of Barrett's epithelium. (e) Biopsy histology of Barrett's esophagus showing characteristic specialized columnar epithelium. (f) OCT image of Barrett's epithelium with disruptions of layered morphology due to multiple crypt- and gland-like structures (arrows).

The OCT image in Figure 18F shows striking differences from those of squamous epithelium (Figure 18C). The uniformly layered structure has been disrupted by the presence of multiple crypt- and gland-like structures as indicated by arrows. The presence of these gland-like morphological features is confirmed with the corresponding histology from the biopsy specimen. This biopsy specimen was interpreted as specialized columnar epithelium consistent with Barrett's esophagus.

Figure 19 shows two representative radial scanning OCT images. Figure 19A is a representative of normal squamous epithelium. The epithelium appears homogeneously backscattering. The arrows in Figure 19A indicate layered structures including the lamina propria and submucosa,

which is more backscattering. The image in Figure 19B is a representative of regions of Barrett's epithelium. The arrow (h) in Figure 19B indicates a heterogeneous region of backscatter which appears similar to that found in metaplastic columnar epithelium. The arrows (c, v, and g) also indicate regions of crypts, vessel and glandular morphology, respectively.

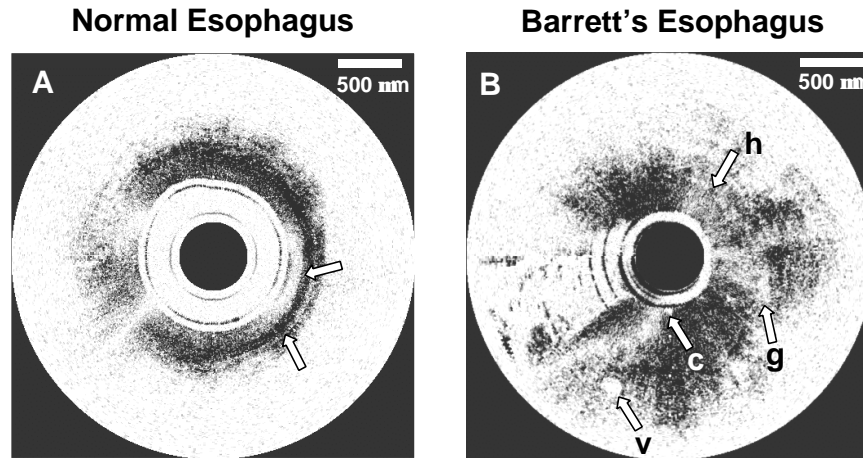


Figure 19: Clinical endoscopic OCT imaging of normal and Barrett's esophagus using radial scanning. Imaging was performed by passing the OCT catheter/probe through the working channel of a standard endoscope. A. Representative image of normal squamous epithelium. Arrows indicate layered structures. B. Representative image of Barrett's epithelium. Arrows indicate heterogeneous scattering regions consistent with crypts (c), glands (g), and vessels (v).

This study reveals the advantages and limitations of linear- and radial-scanning OCT catheter/probes. The linear scanning approach has the advantage that the pixel spacing in the transverse direction is always uniform. This contrasts with the radial imaging approach where the transverse (circumferential) pixel spacing increases with increasing distance from the catheter/probe. The linear catheter can be positioned against the wall of the esophagus, thus not only helping fix the distance to the tissue, but also helping stabilize the catheter/probe position during cardiac or respiratory movements. The rectangular OCT images were freer from distortion and appeared higher in quality than radial scanning OCT images. One major limitation of the linear catheter is that it provides poor coverage of the surface of the esophagus. In comparison the radial catheter could be potentially used for circumferentially imaging the entire lumen. However it is difficult to position and stabilize the radial-imaging catheter/probe in the center of a large lumen such as the human esophagus. Stabilization is possible by collapsing the esophagus around the catheter. But folds in the esophagus developed around the probe prevent the full circumference from being visualized with a single probe placement. In addition the OCT probe could not be viewed endoscopically.

This study has demonstrated that endoscopic OCT resolution can differentiate normal from Barrett's epithelium in real-time based on differences in epithelial architecture. Crypt- and gland-like structures, which disrupted the relatively uniform layers of squamous epithelium, were readily identified, enabling differentiation between normal and Barrett's epithelium. The ability to differentiate normal from Barrett's epithelium suggests that the OCT could be used for screening applications. The results of this study strongly suggest that OCT may be used as an adjunct to endoscopy for screening and surveillance of Barrett's esophagus, in particular in situations where endoscopic visualization is difficult, such as to detect short segment Barrett's or as a follow up to photodynamic therapy to detect residual islands of Barrett's pathology. Future work will focus on developing novel endoscopic OCT catheters that have a higher transverse resolution and that can accommodate a broadband light source for ultrahigh resolution and/or spectroscopic imaging. Development of a balloon imaging catheter/probe for systematic surveillance of the

esophagus will also be of great interest. One major question that still remains unresolved is whether OCT can differentiate high grade and low grade dysplastic changes that occur in conjunction with Barrett's esophagus.

These studies were performed in collaboration with Dr. Jacque van Dam at Stanford Medical School, Dr. Muthoka Mutinga at Brigham and Women's Hospital and Dr. Hiroshi Mashimo at the Massachusetts General Hospital.

Oral Leukoplakia Clinical

Chemoprevention has recently emerged as a promising new approach to the management of treatment of early oropharyngeal neoplastic changes. Head and neck and oral cancer jointly result in over 30,000 new cases with 8,400 deaths annually [37]. Conventional therapy for advanced cancer of these regions typically involves various combinations of surgery and radiation therapy that often result in considerable morbidity. Chemoprevention approaches rely on the detection of early neoplastic changes and attempt to inhibit the transformation of precancerous lesions to invasive cancer. Several pilot studies have shown that oral precancer appears to be responsive to chemoprevention approaches especially using retinoids [45-48]. Standard methods to evaluate the response of oropharyngeal tissue to pharmacological chemoprevention intervention include measurement of leukoplakia lesion surface area and repeated punch biopsies to monitor histological change from baseline to study completion. Serial oral punch biopsies cause discomfort to the patient and suffer from sampling errors. Furthermore, since the tissue is removed in punch biopsy, repeated measures of the same tissue cannot be performed. In contrast to conventional excisional biopsy and histopathology, OCT enables noninvasive and nonexcisional imaging of tissue microstructure to be performed *in situ* and in real time [49, 50]. OCT could provide quantitative assessment of hyperplasia and leukoplakia of the oral mucosa. Because OCT imaging can be performed repeatedly on the same site, it can be used as an objective measure of the progression of oropharyngeal leukoplakia and its response to chemoprevention therapy, thus providing important information to aid the development of chemoprevention therapies. OCT imaging might be used as a screening or "first look" diagnostic for identifying pre-cancerous changes in high risk patient populations.

We have recently begun preliminary imaging studies of oral leukoplakia with a hand-held imaging probe and portable OCT system. The probe permits imaging of the oral cavity to be performed non-invasively and in real time, allowing the effectiveness of pharmacological agents to be monitored *in vivo*. These studies are being performed in collaboration with Dr. James Mulshine of the National Cancer Institute (NCI) in Bethesda, Maryland. Dr. Mulshine's group is investigating the use of ketorolac mouth wash as a potential chemoprevention agent for arresting the progression of leukoplakia to oropharyngeal cancer. Figure 20 (left) shows an example OCT image of normal buccal mucosa. Figure 20 (right) shows an area of leukoplakia on the buccal mucosa of the same patient showing areas of higher scattering and indistinct boundary layers. OCT could provide a quantitative measure of epithelial thickness and subepithelial morphology and therefore allow the effectiveness of chemopreventive agents to be monitored. This data is still very preliminary and we are in the process of corroborating our findings with pathologists.

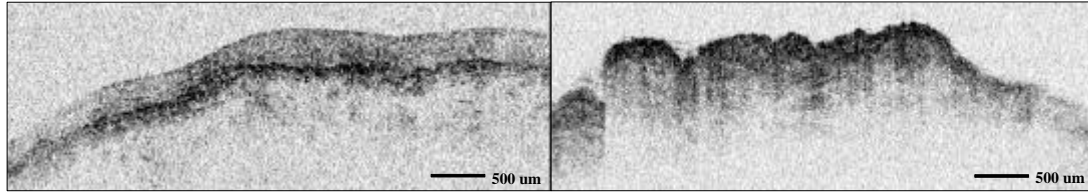


Figure 20: Left: Example of an OCT image of normal buccal mucosa. Right: Area of leukoplakia on the buccal mucosa of the same patient showing areas of higher scattering and indistinct boundary layers. OCT could provide a quantitative measure of epithelial thickness and subepithelial morphology and therefore allow the effectiveness of chemopreventive agents to be monitored.

References

1. Huang, D., E.A. Swanson, C.P. Lin, J.S. Schuman, W.G. Stinson, W. Chang, M.R. Hee, T. Flotte, K. Gregory, C.A. Puliafito and J.G. Fujimoto, "Optical coherence tomography," *Science* 254(5035): p. 1178-1181, 1991.
2. Fujimoto, J.G., C. Pitris, S.A. Boppart and M.E. Brezinski, "Optical coherence tomography: an emerging technology for biomedical imaging and optical biopsy," *Neoplasia* 2(1-2): p. 9-25, 2000.
3. Drexler, W., U. Morgner, F.X. Kärtner, C. Pitris, S.A. Boppart, X.D. Li, E.P. Ippen and J.G. Fujimoto, "In vivo ultrahigh resolution optical coherence tomography," *Optics Letters* 24: p. 1221-1223, 1999.
4. Bouma, B.E., G.J. Tearney, I.P. Bilinsky and B. Golubovic, "Self phase modulated Kerr-lens mode locked Cr:forsterite laser source for optical coherent tomography," *Optics Letters* 21: p. 1839-1841, 1996.
5. Ranka, J.K., R.S. Windeler and A.J. Stentz, "Visible continuum generation in air-silica microstructure optical fibers with anomalous dispersion at 800 nm," *Optics Letters* 25(1): p. 25-7, 2000.
6. Birks, T.A., W.J. Wadsworth and P.S.J. Russell. "Generation of an ultra-broad supercontinuum in tapered fibers (Post-deadline)," presented at the Conference on Lasers and Electro-Optics (CLEO), 2000. San Francisco, CA: OSA.
7. Hartl, I., X.D. Li, C. Chudoba, R.K. Ghanta, T.H. Ko, J.G. Fujimoto, J.K. Ranka and R.S. Windeler, "Ultrahigh-resolution optical coherence tomography using continuum generation in an air-silica microstructure optical fiber," *Optics Letters* 26(9): p. 608-610, 2001.
8. Kulkarni, M.D. and J.A. Izatt, "Spectroscopic optical coherence tomography," *CLEO '96. Summaries of Papers Presented at the Conference on Lasers and Electro Optics* 9(96CH35899): p. 59-60, 1996.
9. Morgner, U., W. Drexler, X. Li, F.X. Kaertner, C. Pitris, S.A. Boppart, E.P. Ippen and J.G. Fujimoto, "Spectroscopic Optical Coherence Tomography," *Optics Letters* 25(2): p. 111-113, 2000.
10. Schmitt, J.M., S.H. Xiang and K.M. Yung, "Differential absorption imaging with optical coherence tomography," *Journal of the Optical Society of America A - Optics Image Science and Vision* 15(9): p. 2288-2296, 1998.
11. Sathyam, U.S., J. B. W. Colston, L.B.D. Silva and M.J. Everett, "Evaluation of optical coherence quantitation of analytes in turbid media by use of two wavelengths," *Applied Optics* 38(10): p. 2097-2104, 1999.
12. Li, X.D., C. Chudoba, T. Ko, C. Pitris and J.G. Fujimoto, "Imaging needle for optical coherence tomography," *Optics Letters* 25, 2000.
13. Hee, M.R., C.A. Puliafito, J.S. Duker, E. Reichel, J.G. Coker, J.R. Wilkins, J.S. Schuman, E.A. Swanson and J.G. Fujimoto, "Topography of diabetic macular edema with optical coherence tomography," *Ophthalmology* 105(2): p. 360-370, 1998.

14. Puliafito, C.A., M.R. Hee, C.P. Lin, E. Reichel, J.S. Schuman, J.S. Duker, J.A. Izatt, E.A. Swanson and J.G. Fujimoto, "Imaging of macular diseases with optical coherence tomography," *Ophthalmology* 102(2): p. 217-229, 1995.
15. Schuman, J.S., T. Pedut-Kloizman, E. Hertzmark, M.R. Hee, J.R. Wilkins, J.G. Coker, C.A. Puliafito, J.G. Fujimoto and E.A. Swanson, "Reproducibility of nerve fiber layer thickness measurements using optical coherence tomography," *Ophthalmology* 103: p. 1889-1898, 1996.
16. Schatz, R.A., "Clinical experience with the Palmaz-Schatz coronary stent," *J Am Coll Cardiol* 17: p. 155B-159B, 1991.
17. Ruygrok, P.N. and P.W. Serruys, "Intracoronary stenting: from concept to custom," *Circulation* 94: p. 882-90, 1996.
18. Yock, P.G., J. Fitzgerald, D.T. Linker and B.A. Angelson, "Intravascular ultrasound guidance for catheter-based intracoronary interventions," *J Amer Coll Cardiol* 17: p. 39B-45B, 1991.
19. Fitzgerald, P.J., A. Oshima, M. Hayase, J.A. Metz, S.R. Bailey, D.S. Baim, M.W. Cleman, E. Deutsch, D.J. Diver, M.B. Leon, J.W. Moses, S.N. Oesterle, P.A. Overlie, C.J. Pepine, R.D. Safian, J. Shani, C.A. Simonton, R.W. Smalling, P.S. Teirstein, J.P. Zidar, A.C. Yeung, R.E. Kuntz and P.G. Yock, "Final results of the Can Routine Ultrasound Influence Stent Routine (CRUISE) study," *Circulation* 102: p. 523-30, 2000.
20. Tearney, G.J., M.E. Brezinski, B.E. Bouma, S.A. Boppart, C. Pitris, J.F. Southern and J.G. Fujimoto, "In vivo endoscopic optical biopsy with optical coherence tomography," *Science* 276(5321): p. 2037-9, 1997.
21. Adams, M.E. and C.J. Wallace, "Quantitative imaging of osteoarthritis," *Seminars in Arthritis and Rheumatism* 20: p. 26-39, 1991.
22. Kelley, W.N., *Textbook of Rheumatology*. 5th ed. Vol. I,II. 1997, Philadelphia: W.B. Sanders.
23. Lozada, C.J. and R.D. Altman, "Chondroprotection in osteoarthritis," *Bull Rheum Dis* 46: p. 5-7, 1997.
24. Buckwalter, J.A. and H.J. Mankin, "Articular cartilage: degeneration and osteoarthritis, repair, regeneration, and transplantation," *Instr Course Lect* 47: p. 487-504, 1998.
25. NIH, NIH Initiative on Osteoarthritis, : <http://www.nih.gov/niams/news/oisg/index.htm>.
26. Chan, W.P., P. Lang, M.P. Stevens, K. Sack, S. Majumdar, D.W. Stoller, C. Basch and K. Genant, "Osteoarthritis of the knee: comparison of radiography, CT, and MR imaging to assess extent and severity," *American Journal of Roentgenology* 157: p. 799-806, 1991.
27. Rubenstein, J.D., J.G. Li, S. Majumdar and R.M. Henkelman, "Image resolution and signal-to-noise requirements for MR imaging of degenerative cartilage," *American Journal of Roentgenology* 169: p. 1089-96, 1997.
28. Loeuille, D., P. Olivier, D. Mainard, P. Gillet, P. Netter and A. Blum, "Review: Magnetic resonance imaging of normal and osteoarthritic cartilage," *Arthritis and Rheumatism* 41: p. 963-75, 1998.
29. Ike, R.W., "Diagnostic arthroscopy," *Baillieres Clinical Rheumatology* 10: p. 495-517, 1996.
30. Parker, S.L., T. Tong, S. Bolden and P.A. Wingo, "Cancer statistics," *CA Cancer J. Clin.* 65: p. 5-27, 1996.
31. Wingo, P.A., S. Landis and L.A. Ries, "An adjustment to the 1997 estimate for new prostate cancer case.," *Journal of Clinical Cancer* 47: p. 239-242, 1997.
32. Hanash, K.A., D.C. Utz, E.N. Look and W.F. Taylor, "Cancer of the prostate: 15 year follow-up.," *Journal of Urology* 107: p. 450-453, 1972.
33. Bocking, A., J. Kiehn and M. Heinzl-Wach, "Combined histologic grading of prostatic carcinoma.," *Cancer* 50: p. 288-294, 1982.
34. Ruijter, E., G. Van Leenders, M. Miller, F. Debruyne and C. Van de Kaa, "Errors in histological grading by prostatic needle biopsy specimens: frequency and predisposing factors.," *Journal of Pathology* 192: p. 229-233, 2000.
35. Montie, J.E. and J.T. Wei, "Artificial neural networks for prostate carcinoma risk assessment.," *Cancer* 91: p. 1647-1652, 2001.

36. D'Amico, A.V., M. Weinstein, X. Li, J.P. Richie and J. Fujimoto, "Optical coherence tomography as a method for identifying benign and malignant microscopic structures in the prostate gland," *Urology* 55(5): p. 783-7, 2000.
37. Landis, S.H., T. Murray, S. Bolden and P.A. Wingo, "Cancer statistics," *CA Cancer J. Clin.* 49: p. 8-31, 1999.
38. Kurman, R.J., P.F. Kaminsky and H.J. Norris, "The behavior of endometrial hyperplasia. A long-term study of "untreated" hyperplasia in 170 patients," *Cancer* 56: p. 403-412, 1985.
39. Anderson, M.C., J.A. Jordan, A.R. Morse and F. Sharpl, *Integrated Colposcopy*. 1996, New York: Chapman and Hall Medical.
40. Phillips, R.W. and R.K.H. Wong, "Barrett's esophagus: natural history, incidence, etiology, and complications," *Gastro. Clinics of North America* 20: p. 791-815, 1991.
41. Sampliner, R.E., "Practice guidelines on the diagnosis, surveillance, and therapy of Barrett's esophagus. The Practice Parameters Committee of the American College of Gastroenterology," *Am J Gastroenterol* 93: p. 1028-32, 1998.
42. Axon, A.T., "Cancer surveillance in ulcerative colitis-- a time for reappraisal," *Gut* 35: p. 587-589, 1994.
43. Falk, G.W., T.W. Rice, J.R. Goldblum and J.E. Richter, "Jumbo biopsy forceps protocol still misses unsuspected cancer in Barrett's esophagus with high-grade dysplasia," 49: p. 170-6, 1999.
44. Adrain, A.L., H.C. Ter, M.J. Cassidy, T.D. Schiano, J.B. Liu and L.S. Miller, "High-resolution endoluminal sonography is a sensitive modality for the identification of Barrett's metaplasia," *Gastrointest Endosc* 46: p. 147-51, 1997.
45. Garewal, H.S., F.L. Meyskens, D. Killen and e. al., "Response of oral leukoplakia to beta carotene," *J. Clin. Oncol.* 8: p. 1715-1720, 1990.
46. Epstein, J.B., F.L. Wong, A. Millner and N.D. Le, "Topical bleomycin treatment of oral leukoplakia: a randomized double-blind clinical trial," *Head and Neck* 16: p. 539-544, 1994.
47. Sankaranarayanan, R., B. Mathew, C. Varghese and e. al., "Chemoprevention of oral leukoplakia with vitamin A and beta carotene: an assessment," *Oral Oncol.* 33: p. 231-236, 1997.
48. Hong, W.K., J. Endicott, L.M. Itri and e. al., "13 cis retinoic acid in the treatment of oral leukoplakia," *New England Journal of Medicine* 315: p. 1501-1505, 1986.
49. Boppart, S.A., B.E. Bouma, C. Pitris, J.F. Southern, M.E. Brezinski and J.G. Fujimoto, "In vivo cellular optical coherence tomography imaging," *Nature Medicine* 4(7): p. 861-5, 1998.
50. Huang, D., J. Wang, C.P. Lin, C.A. Puliafito and J.G. Fujimoto, "Micron-resolution ranging of cornea and anterior chamber by optical reflectometry," *Lasers in Surgery and Med* 11: p. 419-425, 1991.

Publications

1. U. Morgner, W. Drexler, F. X. Kärtner, X. D. Li, C. Pitris, E. P. Ippen, and J. G. Fujimoto, "Spectroscopic optical coherence tomography," *Optics Letters* 25, 111-113, January 15, 2000.
2. J. G. Fujimoto, C. Pitris, S. Boppart, and M. Brezinski, "Optical coherence tomography, an emerging technology for biomedical imaging and optical biopsy," *Neoplasia* 2, 9-25, January 2000.
3. J. G. Fujimoto, W. Drexler, U. Morgner, F. Kärtner, and E. P. Ippen, "Optical coherence tomography: high resolution imaging using echoes of light," *Optics and Photonics News* 11, 24-31, January 2000.
4. C. Pitris, C. Jesser, S. A. Boppart, D. Stamper, M. E. Brezinski, and J. G. Fujimoto, "Feasibility of optical coherence tomography for high resolution imaging of human gastrointestinal tract malignancies," *J. Gastroenterology* 35, 87-92, February 2000.

5. P. Patwari, N. J. Weissman, S. A. Boppart, C. A. Jesser, D. Stamper, J. G. Fujimoto, and M. E. Brezinski, "Assessment of coronary plaque with optical coherence tomography and high frequency ultrasound," *Journal of the American College of Cardiology*, 85, 641-644, March 2000.
6. S. A. Boppart, J. M. Herrmann, and J. G. Fujimoto, "Optical coherence tomography: Applications in surgical diagnosis, guidance and intervention," *Medical Imaging International* 10, 14-20, March-April 2000.
7. A. V. D'Amico, M. Weinstein, X. Li, J. P. Richie, and J. G. Fujimoto, "Optical coherence tomography as a method for identifying benign and malignant microscopic structures in the prostate gland," *Urology* 55, 783-787, 2000.
8. J. Van Dam and J. G. Fujimoto, "Imaging beyond the endoscope," *Gastrointestinal Endoscopy* 51, Part 1, 512-516, 2000.
9. W. Drexler, U. Morgner, R. K. Ghanta, J. S. Schuman, F. X. Kartner, M. R. Hee, E. P. Ippen, and J. G. Fujimoto, "New technology for ultrahigh resolution optical coherence tomography of the retina," in *The Shape of Glaucoma, Quantitative Neural Imaging Techniques*, H. G. Lemij and J. S. Schuman, Eds., pp. 75-104, Kugler Publications, The Hague, Netherlands, 2000.
10. X. D. Li, C. Chudoba, T. Ko, C. Pitris, and J.G. Fujimoto, "Imaging needle for optical coherence tomography," *Optics Letters* 25, October 2000.
11. X. D. Li, S. A. Boppart, J. Van Dam, H. Mashimo, M. Mutinga, W. Drexler, M. Klein, C. Pitris, M. L. Krinsky, M. E. Brezinski, and J. G. Fujimoto, "Current and future endoscopic optical coherence tomography techniques for imaging Barrett's esophagus," *Endoscopy* 32, 921-30, December 2000.
12. W. Drexler, U. Morgner, R. K. Ghanta, F. X. Kärtner, J. S. Schuman, J.G. Fujimoto, "Ultrahigh resolution ophthalmic optical coherence tomography," *Nature Medicine* 7, 502-507, April 2001.
13. I. Hartl, X.D. Li, C. Chudoba, R. Ghanta, T. Ko, J.G. Fujimoto, J. K. Ranka, R. S. Windeler, and A. J. Stentz, "Ultrahigh resolution optical coherence tomography using continuum generation in an air-silica microstructure optical fiber," *Optics Letters* 26, 608-610, May 2001.
14. C. Pitris, K. T. Saunders, J. G. Fujimoto, and M. E. Brezinski, "High resolution imaging of the middle ear with optical coherence tomography, a feasibility study," *Archives of Otolaryngology*, in press.